Dalton Transactions

ROYAL SOCIETY OF CHEMISTRY

COMMUNICATION

View Article Online
View Journal | View Issue

Cite this: *Dalton Trans.*, 2026, **55**, 5893

Received 2nd December 2025,
Accepted 23rd March 2026

DOI: 10.1039/d5dt02879e

rsc.li/dalton

Hybrid sequential processing of mixed Sn–Pb narrow-bandgap perovskite solar cells

Yasemin Saygili, *[a] Federico Ventosinos,[b] Mohammad Dehnavi,[c] Selçuk Yerci,[c,d] Michele Sessolo *[b] and Henk Bolink[b]

Hybrid vapor-solution sequential deposition of perovskites is a well-established method that enables large-area processing of perovskite films and solar cells. In this study, for the first time, we applied the hybrid sequential deposition method to the fabrication of narrow-bandgap mixed Sn–Pb perovskite films. We obtained compact, large-grained perovskite films with power conversion efficiency values exceeding 10% under 1 sun illumination with hole-transport-material-free devices. The applied method eliminates the oxidative degradation risks of solvents during perovskite formation and provides an easy way to develop additive and passivation strategies to improve photovoltaic properties.

Metal halide perovskites have gained considerable attention among the emerging photovoltaic technologies over the last decade. The advancements in perovskite film morphology, composition and device optimization have led to the development of single-junction and tandem perovskite solar cells (PSCs) with remarkable efficiency and promising stability.[1–4] The general ABX_3 perovskite structure allows tuning of the photophysical and chemical properties by employing different compositions of monovalent cations, divalent metals, and halides.[4] Record photovoltaic performance has been mostly obtained when Pb^{2+} occupies the B site; however, partial or full substitution of Sn^{2+} has several advantages. With partial Sn^{2+} substitution, the bandgap (E_g) can be lowered in the energy region of the radiative efficiency limit for single-junction solar cells (approximately 1.34 eV).[5] Sn^{2+}-substituted narrow-bandgap (1.1–1.3 eV) absorbers can also be employed as the rear sub-cells in all-perovskite tandem solar cells.[6,7] In addition, reducing the toxic Pb^{2+} content or full replacement with less toxic Sn^{2+} is reported to reduce the possible health risks.[8,9] However, Sn^{2+} or mixed Sn^{2+}/Pb^{2+} perovskites exhibit poorer optoelectronic properties compared to the Pb^{2+} counterparts.[8,10] Sn^{2+} oxidation to Sn^{4+} appears to be the main challenge in terms of device performance and stability.[8,11,12]

Metal halide perovskite films can be deposited using different methods. Most of these techniques rely on solution processing, either one-step anti-solvent assisted deposition[6,13,14] or two-step spin-coating.[15–18] However, the use of polar aprotic solvents (*e.g.*, dimethylformamide, DMF) in combination with heavy metals and the use of anti-solvents (*e.g.*, chlorobenzene) raise ecotoxicity and health concerns.[19] Besides, solution-processing might be a practical barrier for sustainable, large-area and industrial-scale PSC production.[20] In addition to the aforementioned drawbacks, the interaction of dimethyl sulfoxide (DMSO) with tin halides remains controversial in the literature. In some studies, it was observed that DMSO played a crucial role in slowing down the crystallization and thereby enhancing the crystal quality, while other reports highlighted its detrimental effect on the oxidation of Sn^{2+} to Sn^{4+}.[11,12,21] Alternative thin-film deposition processes to obtain Sn^{2+} or Sn^{2+}/Pb^{2+} narrow bandgap perovskites are vacuum deposition,[22–27] vapor-assisted solution processing[16,28] and hybrid methods.[29,30]

Herein, we applied the well-known hybrid sequential deposition method[31–33] for the first time to fabricate mixed $FA_yMA_{(1-y)}Pb_xSn_{(1-x)}I_3$ perovskite devices. This method is widely studied for mid- and wide-bandgap perovskites,[34,35] enabling high efficiencies without the use of DMF/DMSO, and offering good scalability to large areas. Although Mitzi and co-workers[15] studied this method for Sn-based perovskites in 1998, so far, to the best of our knowledge, no narrow bandgap PSC has been reported using this fabrication method. We first deposited the inorganic $Pb_xSn_{(1-x)}I_2$ films through simultaneous co-evaporation of PbI_2, SnI_2 and SnF_2 in a vacuum chamber. The sublimation rates were monitored through individual microbalance crystal sensors. Depending on the desired nominal Sn/Pb composition, the precursor sublimation rates

[a]*Department of Energy Systems Engineering, Ankara University, Gölbaşı, Ankara 06830, Türkiye. E-mail: ysaygili@ankara.edu.tr*
[b]*Instituto de Ciencia Molecular, Universidad de Valencia, C/Catedrático J. Beltrán 2, 46980 Paterna Valencia, Spain. E-mail: michele.sessolo@uv.es*
[c]*ODTU GUNAM, Middle East Technical University, Çankaya, Ankara 06800, Türkiye*
[d]*Department of Electrical Electronics Engineering, Middle East Technical University, Cankaya, Ankara 06800, Türkiye*

were controlled by manipulating the source temperatures. SnF_2 was employed as a stabilizing additive during evaporation.[36–39] The concentration of SnF_2 was consistently kept low to prevent phase segregation on the perovskite surface[36] (at 4–6% with respect to SnI_2 rate).[24] In the second step, perovskite formation and crystallization are induced by spin coating of an organic cation solution, followed by a rapid annealing step. Hole-transport-material (HTM)-free indium tin oxide (ITO) substrates were used not only to avoid complexity in the device architecture but also because ITO/perovskite heterojunctions are already reported to be stable and energetically well aligned, at least in the case of mixed Sn/Pb PSCs.[40]

In the sequential deposition method, the cation solution plays a key role in the resulting perovskite crystal size and film morphology.[41,42] Therefore, we tested alternative cation solutions employing different solvents, cation concentrations and additives and analyzed the effect through absorbance spectra of the perovskite films. The ultraviolet-visible (UV-vis) absorption spectra for $Pb_{0.5}Sn_{0.5}I_2$ seed film and $FA_{0.7}MA_{0.3}Pb_{0.5}Sn_{0.5}I_3$ perovskite film deposited on ITO are given in Fig. 1(a). While SnF_2 was used as a stabilization agent during the evaporation step, the need for another additive in the cation solution was evaluated. Accordingly, we added metallic Sn powder[7] to the cation solution and examined its effect on the optical properties of the perovskite films. However, the addition of metallic Sn did not produce any significant change in the absorbance spectra of the prepared perovskite films (Fig. S1).

X-ray diffraction (XRD) signals of the $Pb_{0.5}Sn_{0.5}I_2$ seed layer and perovskite film fabricated on ITO are given in Fig. 1(b). The seed film shows a strong peak at 12.6°, indicating crystalline $(Pb/Sn)I_2$ phase.[30] For the perovskite film, the XRD reflections appearing at 14°, 28°, and 43° are associated with the (110), (220), and (330) planes of the perovskite tetragonal crystal structure, respectively.[43] In most cases, the peak at 12.6° disappeared, owing to full conversion to perovskite, but some films still exhibited unconverted $(Pb/Sn)I_2$ content (Fig. S2(a)). In addition to HTM-free ITO substrates, perovskite conversion was also tested on poly(3,4-ethylenedioxythiophene):polystyrene sulfonate (PEDOT:PSS) and poly[bis(4-phenyl)(2,4,6-trimethylphenyl)amine] (PTAA). The effect of substrate choice on perovskite formation was assessed qualitatively using XRD measurements. Some perovskite films employing PEDOT:PSS showed an additional diffraction at 25°, which is attributed to the orthorhombic perovskite structure.[36,38] The rest of the peaks showed an XRD pattern

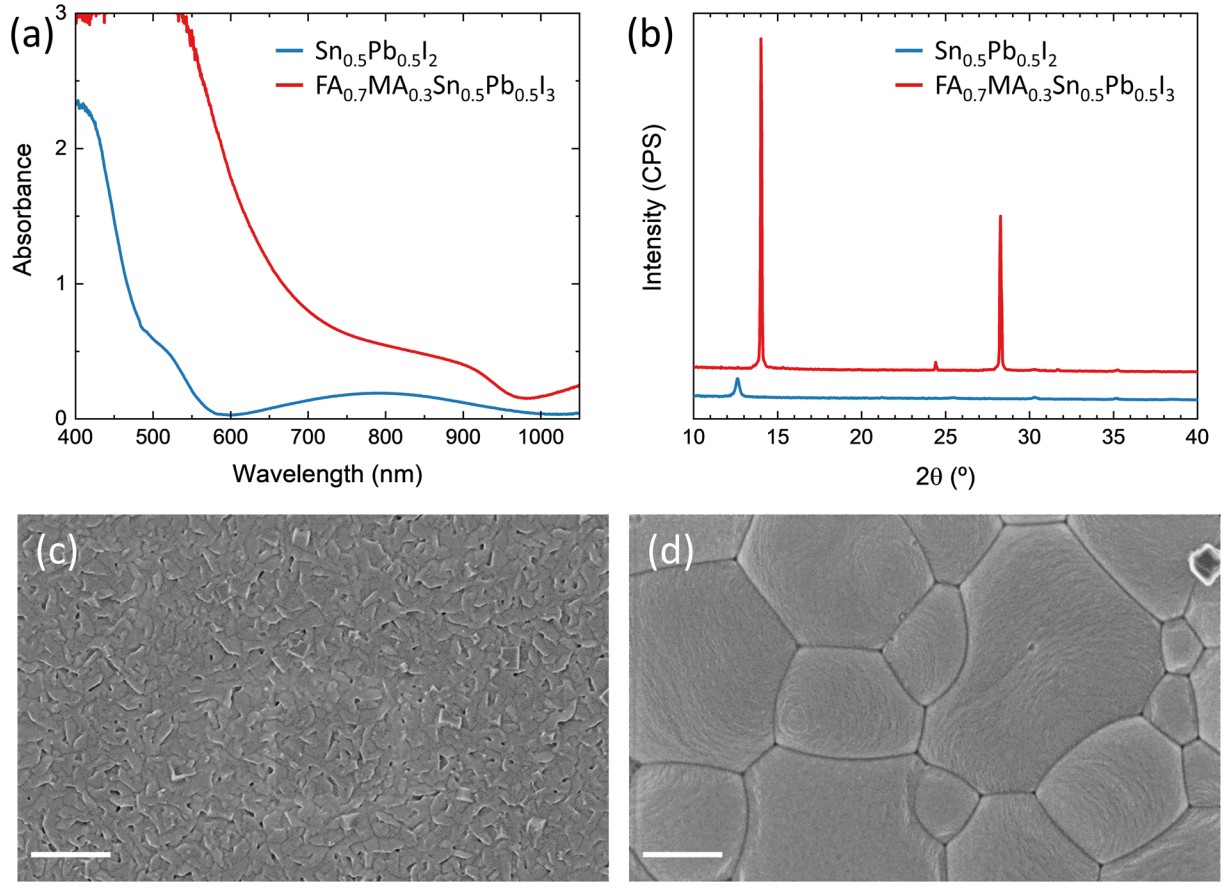

Fig. 1 (a) UV-vis spectra of an evaporated $Pb_{0.5}Sn_{0.5}I_2$ film and fabricated perovskite film. (b) XRD data of the evaporated $Pb_{0.5}Sn0.5I_2$ film and perovskite film. (c) SEM image of the evaporated $Pb_{0.5}Sn_{0.5}I_2$ film. (d) SEM image of the fabricated perovskite film (bar scales 300 nm).

with {110} growth orientation, as in the case of ITO substrates (Fig. S2(b)). The samples employing PTAA exhibited a strong 12.6° diffraction after perovskite conversion, which implies incomplete perovskite formation (Fig. S2(c)). The differences in XRD patterns arising from the choice of substrate can be attributed to the formation of nucleation seeds, wetting behaviour, and diffusion of organic cations into the porous inorganic seed layer during conversion.

Top-view scanning electron microscopy (SEM) images of the inorganic seed layer and perovskite films fabricated on ITO are given in Fig. 1(c) and (d), respectively. The evaporated $Pb_{0.5}Sn_{0.5}I_2$ films exhibit uniform surface coverage with porous morphology. The porous structure of the inorganic film is expected to facilitate cation insertion through the film during the conversion step.[28] The SEM image of the obtained $FA_{0.7}MA_{0.3}Pb_{0.5}Sn_{0.5}I_3$ perovskite films on ITO (Fig. 1(d)) shows high crystallinity with uniform, smooth and defect-free morphology. With the hybrid conversion technique, up to 1.8 μm grain size was obtained, with the average grain size of 1.01 ± 0.47 μm.

Minority carrier diffusion lengths (L_d) were measured using the steady-state photocarrier grating (SSPG) technique.[44,45] Details of the theory behind the technique may be found elsewhere.[46] While this technique was mainly developed to study

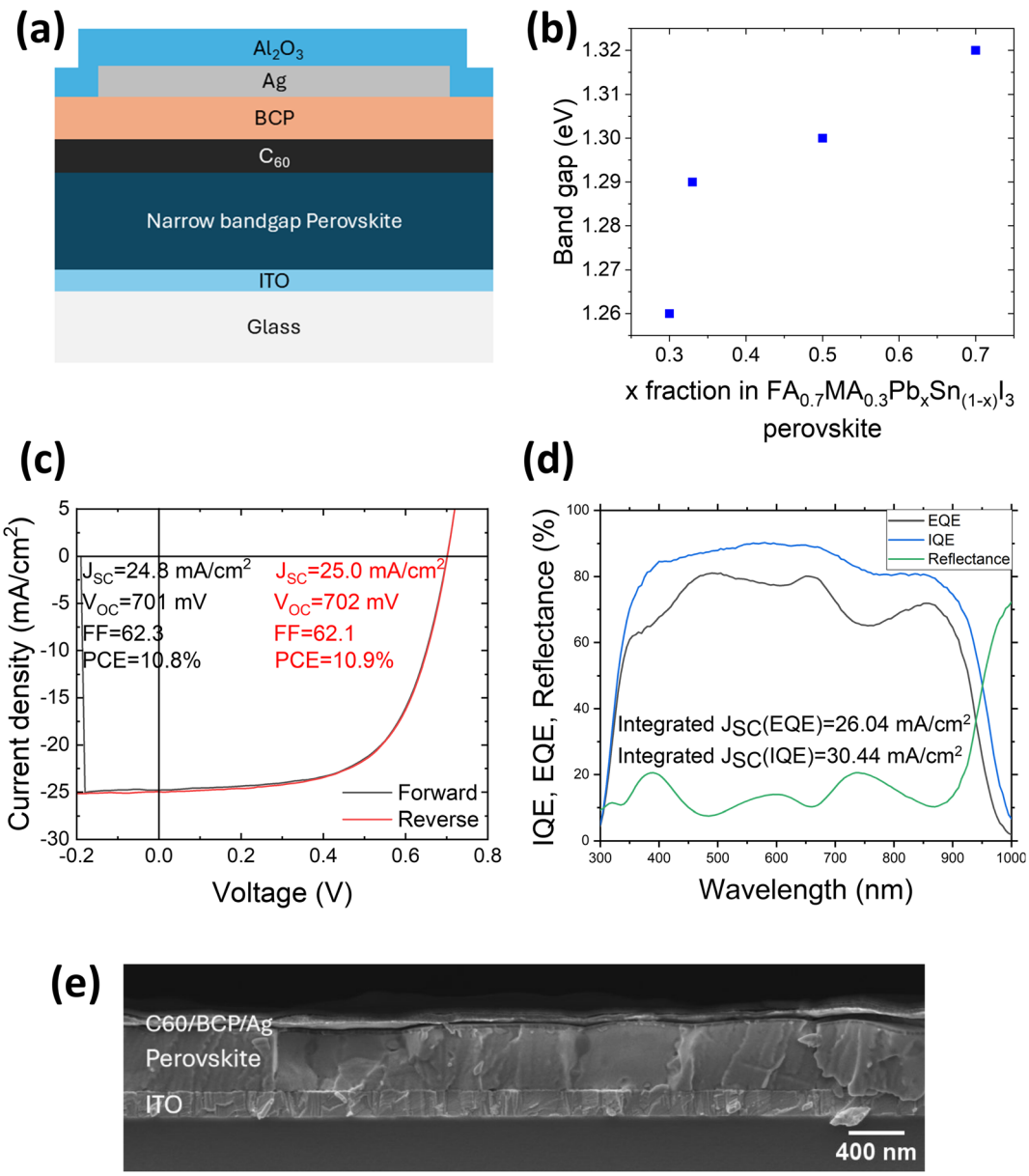

Fig. 2 (a) Scheme of the fabricated devices. (b) Bandgap values derived from the derivative of EQE spectrum for perovskite devices employing different nominal Pb/Sn ratios. Performance metrics of a typical device fabricated through the conversion of evaporated $Pb_{0.5}Sn_{0.5}I_2$ films. (c) *J*–*V* curves measured under standard AM 1.5G illumination. (d) EQE, IQE and reflectance spectra. (e) Cross-sectional SEM image of a typical device.

amorphous silicon films, its applicability to perovskite films has already been addressed.[47–49] As usual with SSPG, the measurements were carried out on samples with coplanar contacts (gold in this case), thus measuring a diffusion length in the lateral plane. Nevertheless, the obtained information is known to be associated with device performance, grain size and recombination mechanisms.[49] For the $FA_{0.7}MA_{0.3}Pb_{0.5}Sn_{0.5}I_3$ film deposited on glass, the ambipolar diffusion lengths (which are dominated by the minority carriers) started around 300 nm for full intensity (giving a generation rate (G) of $G = 1 \times 10^{22}$ cm^{-3} s^{-1}) and increased upon lowering the flux up to 470 nm (for 10% of full flux, see Fig. S3). This dependence of L_d on G has been found for other semiconductors like amorphous silicon,[49] but differs from that reported by Levine *et al.*[47] for their perovskite films ($MAPbI_3$ and $MAPbI_3(Cl)$), where it was found to be constant. Regarding the diffusion length values, we found similar values to the ones reported for $MAPbI_3$ perovskites obtained by solution processing technique,[49,50] and higher than the $MAPbI_3$ films done by co-evaporation in our laboratory, which are around 250 nm for full flux and around 300 nm for 10% of full flux (the SSPG measurement data and the model fitting curves are given in Fig. S4).

The perovskite films formed by the hybrid conversion method were tested in HTM-free p–i–n devices. The devices employed evaporated carbon 60 fullerene (C60) (20 nm)/bathocuproine (BCP) (7 nm) as electron transport layer and Ag metallic contacts, encapsulated with an atomic layer deposition (ALD) of Al_2O_3. A schematic of the fabricated device is given in Fig. 2(a). The effective band gap values as a function of the nominal Pb and Sn content were estimated from the first derivative of the external quantum efficiency (EQE, Fig. 2(b)).[51–53] We obtained the lowest bandgap value of 1.26 eV with the conversion of $Pb_{0.3}Sn_{0.7}I_2$ seed films (normalized EQE plots and a typical photoluminescence (PL) spectrum are provided in Fig. S5 and S6, respectively). Bandgap values tend to increase with increasing nominal Pb content; however, within the range of the studied compositions, we did not observe a clear trend in relation to bandgap bowing behavior.[54] The absence of clear bandgap bowing may be due to the limited composition range and effects related to material defectivity. Higher concentrations of Sn were not studied, as the device performance deteriorated with increasing Sn content. Therefore, the reported bandgap evolution should be interpreted as reflecting a trend with nominal precursor ratios rather than quantitative compositional bandgap mapping. The

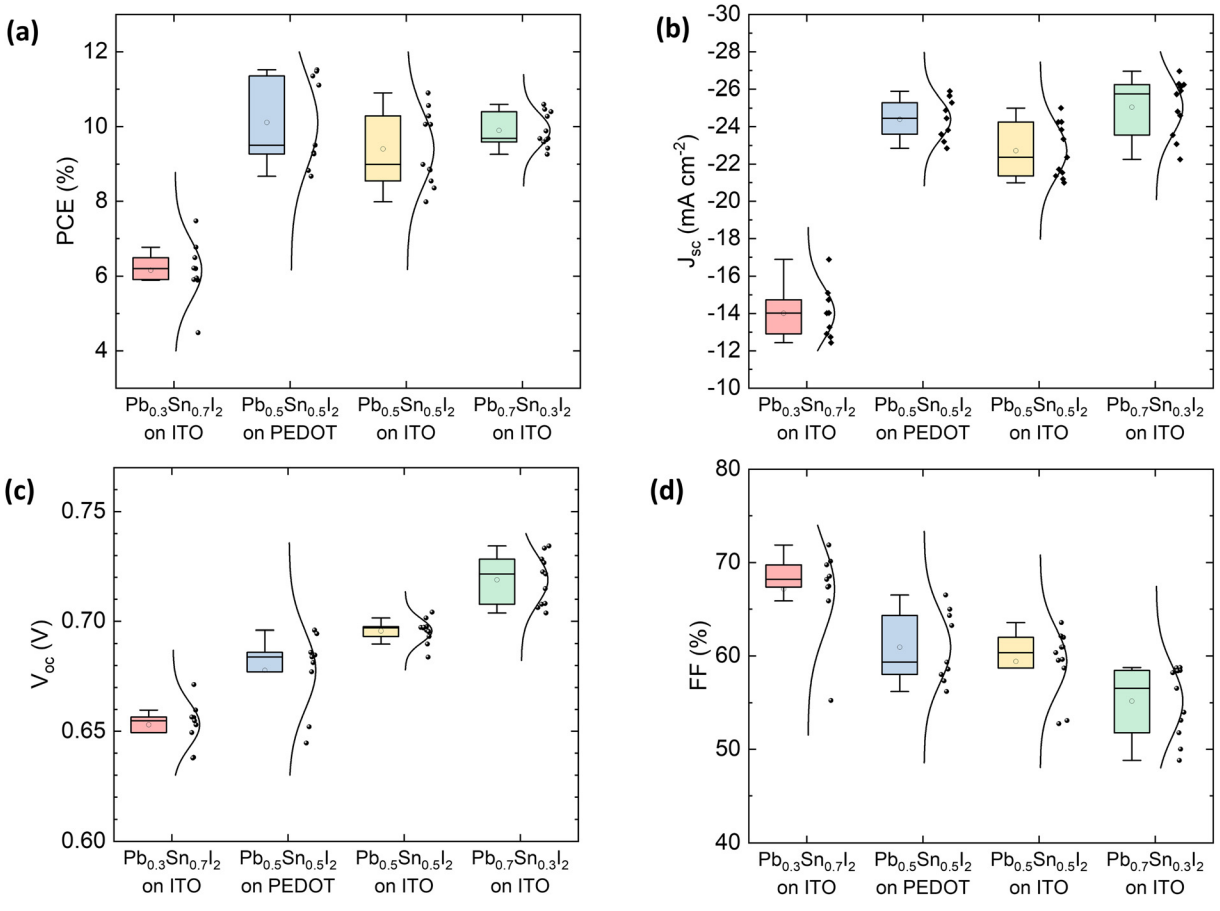

Fig. 3 Statistics of (a) power conversion efficiency, (b) short-circuit current density, (c) open-circuit voltage, and (d) fill factor values of the devices obtained through the conversion of $Pb_xSn_{(1-x)}I_2$ seed films.

optimum photovoltaic performance was typically recorded with perovskite films with a band gap of 1.3 eV, which were obtained through the conversion of $Pb_{0.5}Sn_{0.5}I_2$ inorganic seed films. For the best device within a typical batch, the power conversion efficiency (PCE) was recorded as 10.9% from the photocurrent density *vs.* voltage (*J–V*) curve (reverse scan) under simulated solar illumination (AM 1.5G, 100 mW cm^{-2}), with a short-circuit current density (J_{sc}), open circuit voltage (V_{oc}) and fill factor (FF) of 25.0 mA cm^{-2}, 702 mV and 62.1%, respectively (Fig. 2(c)). The external quantum efficiency (EQE), internal quantum efficiency (IQE), and reflectance (*R*) spectra of the same device are given in (Fig. 2(d)). The integrated EQE spectrum for the same device remains in accordance with the J_{sc} value obtained from the *J–V* curves (the mismatch can be related to the difference in equipment light sources). By accounting for the reflectance, the integrated IQE spectrum gives a maximum J_{sc} of 30.44 mA cm^{-2}, which indicates that device performance can be enhanced not only by minimizing reflectance losses but also by improving charge collection within the device. The lower EQE at long wavelengths also indicates insufficient perovskite thickness, which was measured as 429 ± 22 nm, as shown in the cross-sectional SEM view of a typical device (Fig. 2(e)). Although the devices fabricated on PEDOT:PSS substrates resulted in efficiency values reaching over 11% (Fig. S7), further analyses were carried out on HTM-free devices, considering the stability issues reported for PEDOT:PSS and for simplicity in device architecture.[40] With PTAA (Fig. S8), the *J–V* curves exhibited the S-shaped characteristic, independent of the employed HTM thickness. For these samples, we presume that the unconverted $(Pb/Sn)I_2$ acts as an insulating domain or has unfavorable band alignment, which obstructs the charge collection and, accordingly, the device performance.[55] With PTAA, the resulting PCE values were lower compared to those reported for one-step solution-processed mixed PSC.[18]

Perovskite devices employing different nominal Sn/Pb ratios were fabricated through the conversion of $Pb_xSn_{(1-x)}I_2$ seed layers. The photovoltaic parameters are summarized by the statistical box charts in Fig. 3. Solar cells with $FA_{0.7}MA_{0.3}Pb_{0.5}Sn_{0.5}I_3$ films on PEDOT:PSS have higher PCE values compared to the HTM-free counterparts, which can be attributed to a better energy alignment and/or better film crystallization. Although the EQE onset spectra (Fig. S5) exhibit a red shift with increasing nominal Sn/Pb ratios, the corresponding bandgap reduction is more pronounced at lower Pb fractions. Conversion of $Pb_{0.3}Sn_{0.7}I_2$ film yields a bandgap of approximately 1.26 eV, whereas the conversions with $Pb_{0.5}Sn_{0.5}I_2$ and $Pb_{0.7}Sn_{0.3}I_2$ films result in bandgaps of 1.3 eV and 1.32 eV, respectively. This nonlinear trend suggests that, from a detailed balance perspective, performance differences attributed solely to bandgap variation may be masked by statistical fluctuations.

The theoretical short-circuit current density from the Shockley–Queisser (SQ)[56] limit for a bandgap of 1.32 eV is 35.44 mA cm^{-2}, while for 1.3 eV, it is slightly higher at 35.82 mA cm^{-2}. In our experimental data, however, the device with a 1.3 eV bandgap exhibits a marginally lower J_{sc} (mean value of 22.7 mA cm^{-2}, compared to 25.1 mA cm^{-2} for the higher bandgap device). This variation, however, falls within the experimental statistical spread. According to Fig. 3(b), the J_{sc} values show an increasing trend for higher nominal Pb/Sn ratios. As depicted in Fig. 3(c), the open-circuit voltage follows the expected detailed balance trend, with slightly higher values observed for the higher bandgap device (0.72 V to 0.70 V of mean values). Nevertheless, the experimental spread in V_{oc} values is sufficiently large that we cannot conclusively attribute these differences to bandgap and conduction band edge[54] variations alone. We also illustrated the *J–V* characteristics of the solar cells employing $FA_{0.7}MA_{0.3}Pb_{0.3}Sn_{0.7}I_3$, $FA_{0.7}MA_{0.3}Pb_{0.5}Sn_{0.5}I_3$, and $FA_{0.7}MA_{0.3}Pb_{0.7}Sn_{0.3}I_3$ perovskites on ITO using SCAPS-1D.[57] The set values for the parameters

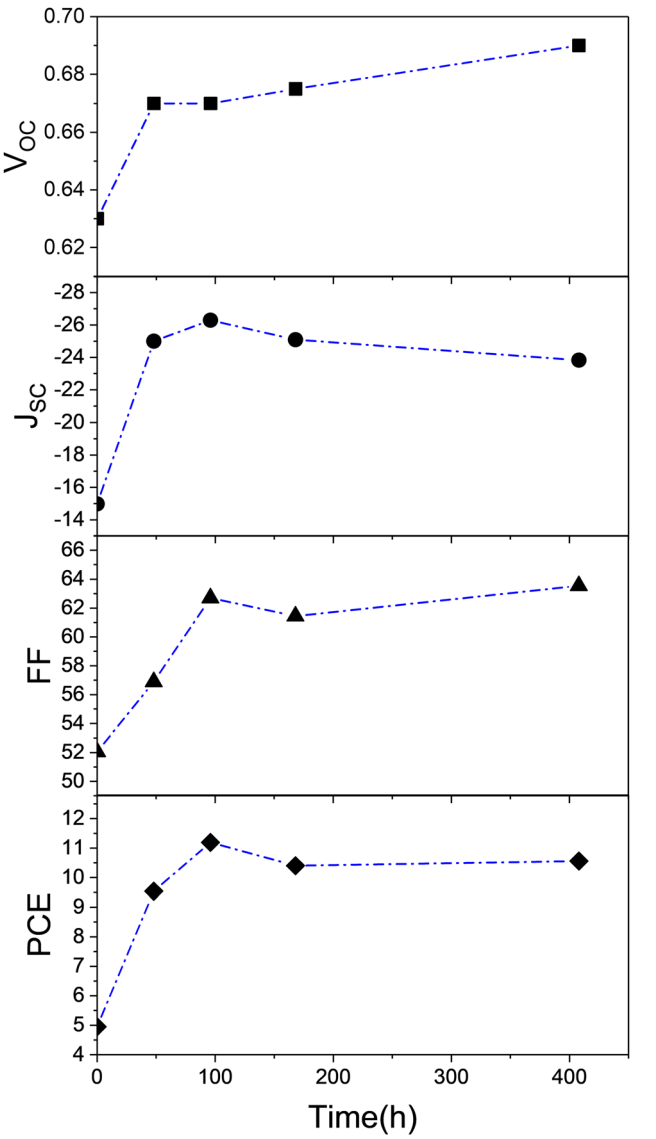

Fig. 4 Change of photovoltaic parameters of an Al_2O_3 encapsulated perovskite solar cell fabricated on ITO as a function of time (samples stored in the dark and under inert atmosphere).

and the device metrics obtained through the simulations are given in Tables S1–S4 and Fig. S9.

The stability of the encapsulated $FA_{0.7}MA_{0.3}Pb_{0.5}Sn_{0.5}I_3$ PSCs stored in a dark glovebox atmosphere was monitored through *J–V* measurements (Fig. 4). The photovoltaic parameters exhibited improvement (most significantly, the current density values) within a couple of days after fabrication and then stayed mostly stable for 500 h. Although the origin is unclear, based on the similar trends reported in literature, this initial enhancement in the PCE value is consistent with reports of aging-induced reorganization[58,59] and self-healing processes[60] reported for polycrystalline perovskites.[58–60] Self-healing in Sn-based solution-processed perovskites is related to the reversible chemical effects, *i.e.*, the reduction of Sn^{4+} back to Sn^{2+}.[60] Selectivity of coalescence is reported to be favorable when the degree of misorientation at the grain boundaries is low, which conforms with our case (Fig. 1(b)).[59] We can speculate that spontaneous coalescence and, similarly, additive-induced Ostwald ripening[61,62] can be used in Pb/Sn mixed perovskites to alleviate the drawbacks of fast crystallization and resulting poor film morphologies.

In conclusion, a hybrid sequential deposition method was effectively used for the first time for fabricating narrow-bandgap mixed Pb/Sn perovskite solar cells. With this method, we obtained PCE values reaching over 10% both with HTM-free and PEDOT:PSS substrates. We expect that with certain additives and surface passivation strategies, the photovoltaic performance can be enhanced further. Avoiding the use of DMF and DMSO during perovskite formation provides a more environmentally friendly approach. Also, eliminating DMSO might help prevent Sn oxidation to Sn(IV). We expect that our findings can be used as a starting point for the manufacturing of mixed Pb/Sn perovskites, especially for tandem solar cell applications.

Conflicts of interest

The authors declare no conflicts of interest.

Data availability

The data supporting this article have been included as part of the supplementary information (SI). In addition, the simulation files and the related data for this work are accessible at https://github.com/ODTUGUNAM/Mixed-SnPb-Perovskite-Simulation.

Supplementary information: Experimental methods, UV-Vis spectra, XRD data, SSPG analysis, EQE spectra, PL spectra, Current density–photovoltage curves, Simulation tables. See DOI: https://doi.org/10.1039/d5dt02879e.

Acknowledgements

Y. S. is grateful for the financial support of the project no. 121C038 from the co-funded Brain Circulation Scheme (CoCirculation2) Project of the program introduced by Turkish Scientific and Technological Research Council (TÜBİTAK-2236) and European Commission Horizon 2020 Marie Skłodowska-Curie Actions under contract FP7-PEOPLE-2011-COFUND. This work was carried out within the framework of the REFORM project (CETP-2022-00348), funded by the Clean Energy Transition Partnership (CETPartnership) Joint Call 2022, co-funded by the European Union's Horizon Europe programme (Grant Agreement No. 101069750), and by national funding bodies including the Agencia Estatal de Investigación (AEI, Spain, PCI2023-145969-2) and TÜBİTAK (Turkey, 223N002). M. S. acknowledges funding from the Ministry of Science and Innovation (MCIN) and the AEI for project PCI2023-145969-2 funded by MICIU/AEI/10.13039/501100011033 and co-funded by the European Union. Dr. Cristina Roldán-Carmona is acknowledged for SEM measurements. Dr. Marc Burgelman is acknowledged for providing SCAPS-1D simulation software.

References

1 H.-S. Kim, C.-R. Lee, J.-H. Im, K.-B. Lee, T. Moehl, A. Marchioro, S.-J. Moon, R. Humphry-Baker, J.-H. Yum, J. E. Moser, M. Grätzel and N.-G. Park, Lead Iodide Perovskite Sensitized All-Solid-State Submicron Thin Film Mesoscopic Solar Cell with Efficiency Exceeding 9%, *Sci. Rep.*, 2012, **2**, 591, DOI: 10.1038/srep00591.

2 https://www.nrel.gov/pv/assets/pdfs/cell-pv-eff-emergingpv.pdf, accessed on 25.10.2025.

3 M. A. Green, E. D. Dunlop, M. Yoshita, N. Kopidakis, K. Bothe, G. Siefer, D. Hinken, M. Rauer, J. Hohl-Ebinger and X. Hao, Solar Cell Efficiency Tables (Version 64), *Prog. Photovoltaics*, 2024, **32**(7), 425–441, DOI: 10.1002/pip.3831.

4 H. S. Kim, A. Hagfeldt and N. G. Park, Morphological and Compositional Progress in Halide Perovskite Solar Cells, *Chem. Commun.*, 2019, **55**(9), 1192–1200, DOI: 10.1039/c8cc08653b.

5 K. Dey, B. Roose and S. D. Stranks, Optoelectronic Properties of Low-Bandgap Halide Perovskites for Solar Cell Applications, *Adv. Mater.*, 2021, **33**(40), 2102300, DOI: 10.1002/adma.202102300.

6 C. Wang, Y. Zhao, T. Ma, Y. An, R. He, J. Zhu, C. Chen, S. Ren, F. Fu, D. Zhao and X. Li, A Universal Close-Space Annealing Strategy towards High-Quality Perovskite Absorbers Enabling Efficient All-Perovskite Tandem Solar Cells, *Nat. Energy*, 2022, **7**(8), 744–753, DOI: 10.1038/s41560-022-01076-9.

7 R. Lin, K. Xiao, Z. Qin, Q. Han, C. Zhang, M. Wei, M. I. Saidaminov, Y. Gao, J. Xu, M. Xiao, A. Li, J. Zhu, E. H. Sargent and H. Tan, Monolithic All-Perovskite Tandem Solar Cells with 24.8% Efficiency Exploiting Comproportionation to Suppress Sn(Ii) Oxidation in Precursor Ink, *Nat. Energy*, 2019, **4**(10), 864–873, DOI: 10.1038/s41560-019-0466-3.

8 E. L. Lim, A. Hagfeldt and D. Bi, Toward Highly Efficient and Stable Sn2+ and Mixed Pb2+/Sn2+ based Halide Perovskite Solar Cells through Device Engineering, *Energy Environ. Sci.*, 2021, 3256–3300, DOI: 10.1039/d0ee03368e, Royal Society of Chemistry June 1.

9 J. Li, H. L. Cao, W. B. Jiao, Q. Wang, M. Wei, I. Cantone, J. Lü and A. Abate, Biological Impact of Lead from Halide Perovskites Reveals the Risk of Introducing a Safe Threshold, *Nat. Commun.*, 2020, **11**(1), 310, DOI: 10.1038/s41467-019-13910-y.

10 Y. Li, W. Sun, W. Yan, S. Ye, H. Rao, H. Peng, Z. Zhao, Z. Bian, Z. Liu, H. Zhou and C. Huang, 50% Sn-Based Planar Perovskite Solar Cell with Power Conversion Efficiency up to 13.6%, *Adv. Energy Mater.*, 2016, **6**(24), 1601353, DOI: 10.1002/aenm.201601353.

11 M. I. Saidaminov, I. Spanopoulos, J. Abed, W. Ke, J. Wicks, M. G. Kanatzidis and E. H. Sargent, Conventional Solvent Oxidizes Sn(II) in Perovskite Inks, *ACS Energy Lett.*, 2020, 1153–1155, DOI: 10.1021/acsenergylett.0c00402, American Chemical Society April 10.

12 J. Pascual, G. Nasti, M. H. Aldamasy, J. A. Smith, M. Flatken, N. Phung, D. Di Girolamo, S. H. Turren-Cruz, M. Li, A. Dallmann, R. Avolio and A. Abate, Origin of Sn(Ii) Oxidation in Tin Halide Perovskites, *Mater. Adv.*, 2020, **1**(5), 1066–1070, DOI: 10.1039/d0ma00245c.

13 S. Hu, K. Otsuka, R. Murdey, T. Nakamura, M. A. Truong, T. Yamada, T. Handa, K. Matsuda, K. Nakano, A. Sato, K. Marumoto, K. Tajima, Y. Kanemitsu and A. Wakamiya, Optimized Carrier Extraction at Interfaces for 23.6% Efficient Tin-Lead Perovskite Solar Cells, *Energy Environ. Sci.*, 2022, **15**, 2096–2107, DOI: 10.1039/d2ee00288d.

14 K. Xiao, R. Lin, Q. Han, Y. Hou, Z. Qin, H. T. Nguyen, J. Wen, M. Wei, V. Yeddu, M. I. Saidaminov, Y. Gao, X. Luo, Y. Wang, H. Gao, C. Zhang, J. Xu, J. Zhu, E. H. Sargent and H. Tan, All-Perovskite Tandem Solar Cells with 24.2% Certified Efficiency and Area over 1 Cm2 Using Surface-Anchoring Zwitterionic Antioxidant, *Nat. Energy*, 2020, **5**(11), 870–880, DOI: 10.1038/s41560-020-00705-5.

15 K. Liang, D. B. Mitzi and M. T. Prikas, *Synthesis and Characterization of Organic-Inorganic Perovskite Thin Films Prepared Using a Versatile Two-Step Dipping Technique*, 1998. https://pubs.acs.org/sharingguidelines.

16 T. Yokoyama, D. H. Cao, C. C. Stoumpos, T. B. Song, Y. Sato, S. Aramaki and M. G. Kanatzidis, Overcoming Short-Circuit in Lead-Free $CH_3NH3SnI3$ Perovskite Solar Cells via Kinetically Controlled Gas-Solid Reaction Film Fabrication Process, *J. Phys. Chem. Lett.*, 2016, 7(5), 776–782, DOI: 10.1021/acs.jpclett.6b00118.

17 J. Wang, K. Datta, J. Li, M. A. Verheijen, D. Zhang, M. M. Wienk and R. A. J. Janssen, Understanding the Film Formation Kinetics of Sequential Deposited Narrow-Bandgap Pb–Sn Hybrid Perovskite Films, *Adv. Energy Mater.*, 2020, **10**(22), 2000566, DOI: 10.1002/aenm.202000566.

18 Y. Wang, W. Fu, J. Yan, J. Chen, W. Yang and H. Chen, Low-Bandgap Mixed Tin-Lead Iodide Perovskite with Large Grains for High Performance Solar Cells, *J. Mater. Chem. A*, 2018, **6**(27), 13090–13095, DOI: 10.1039/c8ta03054e.

19 H. S. Kim, Y. J. An, J. Il Kwak, H. J. Kim, H. S. Jung and N. G. Park, Sustainable Green Process for Environmentally Viable Perovskite Solar Cells, *ACS Energy Lett.*, 2022, **7**(3), 1154–1177, DOI: 10.1021/acsenergylett.1c02836.

20 N. G. Park, Green Solvent for Perovskite Solar Cell Production, *Nat. Sustain.*, 2021, **4**, 192–193, DOI: 10.1038/s41893-020-00647-6.

21 G. Nasti, M. H. Aldamasy, M. A. Flatken, P. Musto, P. Matczak, A. Dallmann, A. Hoell, A. Musiienko, H. Hempel, E. Aktas, D. Di Girolamo, J. Pascual, G. Li, M. Li, L. V. Mercaldo, P. D. Veneri and A. Abate, Pyridine Controlled Tin Perovskite Crystallization, *ACS Energy Lett.*, 2022, **7**(10), 3197–3203, DOI: 10.1021/acsenergylett.2c01749.

22 A. M. Igual-Muñoz, A. Castillo, C. Dreessen, P. P. Boix and H. J. Bolink, Vacuum-Deposited Multication Tin-Lead Perovskite Solar Cells, *ACS Appl. Energy Mater.*, 2020, **3**(3), 2755–2761, DOI: 10.1021/acsaem.9b02413.

23 J. M. Ball, L. Buizza, H. C. Sansom, M. D. Farrar, M. T. Klug, J. Borchert, J. Patel, L. M. Herz, M. B. Johnston and H. J. Snaith, Dual-Source Coevaporation of Low-Bandgap FA1-XCsxSn1-YPbyI3 Perovskites for Photovoltaics, *ACS Energy Lett.*, 2019, **4**(11), 2748–2756, DOI: 10.1021/acsenergylett.9b01855.

24 A. M. Igual-Muñoz, J. Ávila, P. P. Boix and H. J. Bolink, FAPb0.5Sn0.5I3: A Narrow Bandgap Perovskite Synthesized through Evaporation Methods for Solar Cell Applications, *Sol. RRL*, 2020, **4**(2), 1900283, DOI: 10.1002/solr.201900283.

25 T. Roh, Y. Reo, S. Heo, G. Park, W. Yang, B. Ham, J. An, J.-H. Jung, S.-H. Baek, R.-H. Baek, C.-J. Kim and Y.-Y. Noh, Growth of Tin Halide Perovskite Film on Two-Dimensional Hexagonal Boron Nitride via Thermal Evaporation, *ACS Energy Lett.*, 2025, **10**(10), 5084–5092, DOI: 10.1021/acsenergylett.5c02309.

26 W. Yang, W. Park, Y. Reo, S. Yoo, S. Cho, H. Kim, S. Ryu and Y.-Y. Noh, Additive-Free Thermally Evaporated Tin Halide Perovskite Transistors, *Mater. Sci. Eng., R*, 2026, **168**, 101141, DOI: 10.1016/j.mser.2025.101141.

27 Y. Reo, T. Zou, T. Choi, S. Kim, J.-Y. Go, T. Roh, H. Ryu, Y.-S. Kim, A. Liu, H. Zhu and Y.-Y. Noh, Vapour-Deposited High-Performance Tin Perovskite Transistors, *Nat. Electron.*, 2025, **8**(5), 403–410, DOI: 10.1038/s41928-025-01380-8.

28 P. Wang, F. Li, K.-J. Jiang, Y. Zhang, H. Fan, Y. Zhang, Y. Miao, J.-H. Huang, C. Gao, X. Zhou, F. Wang, L.-M. Yang, C. Zhan and Y. Song, Ion Exchange/Insertion Reactions for Fabrication of Efficient Methylammonium Tin Iodide Perovskite Solar Cells, *Adv. Sci.*, 2020, **7**(9), 1903047, DOI: 10.1002/advs.201903047.

29 J. Xi, H. Duim, M. Pitaro, K. Gahlot, J. Dong, G. Portale and M. A. Loi, Scalable, Template Driven Formation of Highly Crystalline Lead-Tin Halide Perovskite Films, *Adv. Funct. Mater.*, 2021, **31**(46), 2105734, DOI: 10.1002/adfm.202105734.

30 M. M. Tavakoli, S. M. Zakeeruddin, M. Grätzel and Z. Fan, Large-Grain Tin-Rich Perovskite Films for Efficient Solar Cells via Metal Alloying Technique, *Adv. Mater.*, 2018, **30**(11), 1705998, DOI: 10.1002/adma.201705998.
31 J. Werner, C. H. Weng, A. Walter, L. Fesquet, J. P. Seif, S. De Wolf, B. Niesen and C. Ballif, Efficient Monolithic Perovskite/Silicon Tandem Solar Cell with Cell Area >1 Cm2, *J. Phys. Chem. Lett.*, 2016, **7**(1), 161–166, DOI: 10.1021/acs.jpclett.5b02686.
32 F. Fu, T. Feurer, T. P. Weiss, S. Pisoni, E. Avancini, C. Andres, S. Buecheler and A. N. Tiwari, High-Efficiency Inverted Semi-Transparent Planar Perovskite Solar Cells in Substrate Configuration, *Nat. Energy*, 2017, **2**(1), 16190, DOI: 10.1038/nenergy.2016.190.
33 F. Sahli, J. Werner, B. A. Kamino, M. Bräuninger, R. Monnard, B. Paviet-Salomon, L. Barraud, L. Ding, J. J. Diaz Leon, D. Sacchetto, G. Cattaneo, M. Despeisse, M. Boccard, S. Nicolay, Q. Jeangros, B. Niesen and C. Ballif, Fully Textured Monolithic Perovskite/Silicon Tandem Solar Cells with 25.2% Power Conversion Efficiency, *Nat. Mater.*, 2018, **17**(9), 820–826, DOI: 10.1038/s41563-018-0115-4.
34 W. Soltanpoor, C. Dreessen, M. C. Sahiner, I. Susic, A. Z. Afshord, V. S. Chirvony, P. P. Boix, G. Gunbas, S. Yerci and H. J. Bolink, Hybrid Vapor-Solution Sequentially Deposited Mixed-Halide Perovskite Solar Cells, *ACS Appl. Energy Mater.*, 2020, **3**(9), 8257–8265, DOI: 10.1021/acsaem.0c00686.
35 A. Z. Afshord, B. E. Uzuner, W. Soltanpoor, S. H. Sedani, T. Aernouts, G. Gunbas, Y. Kuang and S. Yerci, Efficient and Stable Inverted Wide-Bandgap Perovskite Solar Cells and Modules Enabled by Hybrid Evaporation-Solution Method, *Adv. Funct. Mater.*, 2023, **33**(31), 2301695, DOI: 10.1002/adfm.202301695.
36 W. Liao, D. Zhao, Y. Yu, C. R. Grice, C. Wang, A. J. Cimaroli, P. Schulz, W. Meng, K. Zhu, R.-G. Xiong and Y. Yan, Lead-Free Inverted Planar Formamidinium Tin Triiodide Perovskite Solar Cells Achieving Power Conversion Efficiencies up to 6.22%, *Adv. Mater.*, 2016, **28**(42), 9333–9340, DOI: 10.1002/adma.201602992.
37 S. Gupta, T. Bendikov, G. Hodes and D. Cahen, CsSnBr3, A Lead-Free Halide Perovskite for Long-Term Solar Cell Application: Insights on SnF2 Addition, *ACS Energy Lett.*, 2016, **1**(5), 1028–1033, DOI: 10.1021/acsenergylett.6b00402.
38 T. M. Koh, T. Krishnamoorthy, N. Yantara, C. Shi, W. L. Leong, P. P. Boix, A. C. Grimsdale, S. G. Mhaisalkar and N. Mathews, Formamidinium Tin-Based Perovskite with Low Eg for Photovoltaic Applications, *J. Mater. Chem. A*, 2015, **3**(29), 14996–15000, DOI: 10.1039/C5TA00190K.
39 M. H. Kumar, S. Dharani, W. L. Leong, P. P. Boix, R. R. Prabhakar, T. Baikie, C. Shi, H. Ding, R. Ramesh, M. Asta, M. Graetzel, S. G. Mhaisalkar and N. Mathews, Lead-Free Halide Perovskite Solar Cells with High Photocurrents Realized Through Vacancy Modulation, *Adv. Mater.*, 2014, **26**(41), 7122–7127, DOI: 10.1002/adma.201401991.
40 R. Prasanna, T. Leijtens, S. P. Dunfield, J. A. Raiford, E. J. Wolf, S. A. Swifter, J. Werner, G. E. Eperon, C. de Paula, A. F. Palmstrom, C. C. Boyd, M. F. A. M. van Hest, S. F. Bent, G. Teeter, J. J. Berry and M. D. McGehee, Design of Low Bandgap Tin–Lead Halide Perovskite Solar Cells to Achieve Thermal, Atmospheric and Operational Stability, *Nat. Energy*, 2019, **4**(11), 939–947, DOI: 10.1038/s41560-019-0471-6.
41 J. Burschka, N. Pellet, S. J. Moon, R. Humphry-Baker, P. Gao, M. K. Nazeeruddin and M. Grätzel, Sequential Deposition as a Route to High-Performance Perovskite-Sensitized Solar Cells, *Nature*, 2013, **499**(7458), 316–319, DOI: 10.1038/nature12340.
42 J. H. Im, I. H. Jang, N. Pellet, M. Grätzel and N. G. Park, Growth of CH_3 NH3 PbI3 Cuboids with Controlled Size for High-Efficiency Perovskite Solar Cells, *Nat. Nanotechnol.*, 2014, **9**(11), 927–932, DOI: 10.1038/nnano.2014.181.
43 B. Zhao, M. Abdi-Jalebi, M. Tabachnyk, H. Glass, V. S. Kamboj, W. Nie, A. J. Pearson, Y. Puttisong, K. C. Gödel, H. E. Beere, D. A. Ritchie, A. D. Mohite, S. E. Dutton, R. H. Friend and A. Sadhanala, High Open-Circuit Voltages in Tin-Rich Low-Bandgap Perovskite-Based Planar Heterojunction Photovoltaics, *Adv. Mater.*, 2017, **29**(2), 1604744, DOI: 10.1002/adma.201604744.
44 D. Ritter, E. Zeldov and K. Weiser, Steady–state Photocarrier Grating Technique for Diffusion Length Measurement in Photoconductive Insulators, *Appl. Phys. Lett.*, 1986, **49**(13), 791–793, DOI: 10.1063/1.97548.
45 D. Ritter, K. Weiser and E. Zeldov, Steady–state Photocarrier Grating Technique for Diffusion–length Measurement in Semiconductors: Theory and Experimental Results for Amorphous Silicon and Semi–insulating GaAs, *J. Appl. Phys.*, 1987, **62**(11), 4563–4570, DOI: 10.1063/1.339051.
46 R. Brüggemann, Steady-State Photocarrier Grating Technique for the Minority-Carrier Characterisation of Thin-Film Semiconductors, *J. Phys.: Conf. Ser.*, 2010, **253**(1), 12081, DOI: 10.1088/1742-6596/253/1/012081.
47 I. Levine, S. Gupta, T. M. Brenner, D. Azulay, O. Millo, G. Hodes, D. Cahen and I. Balberg, Mobility–Lifetime Products in MAPbI3 Films, *J. Phys. Chem. Lett.*, 2016, **7**(24), 5219–5226, DOI: 10.1021/acs.jpclett.6b02287.
48 L. Christophe, Study of Transport Parameters and Defect States in Thin Film Perovskites under Different Environments – Air or Vacuum – and after Light-Soaking, *EPJ Photovoltaics*, 2020, **11**, 5, DOI: 10.1051/epjpv/2019009.
49 G. W. P. Adhyaksa, L. W. Veldhuizen, Y. Kuang, S. Brittman, R. E. I. Schropp and E. C. Garnett, Carrier Diffusion Lengths in Hybrid Perovskites: Processing, Composition, Aging, and Surface Passivation Effects, *Chem. Mater.*, 2016, **28**(15), 5259–5263, DOI: 10.1021/acs.chemmater.6b00466.
50 I. Levine, S. Gupta, A. Bera, D. Ceratti, G. Hodes, D. Cahen, D. Guo, T. J. Savenije, J. Ávila, H. J. Bolink, O. Millo, D. Azulay and I. Balberg, Can We Use Time-Resolved Measurements to Get Steady-State Transport Data for

Halide Perovskites?, *J. Appl. Phys.*, 2018, **124**(10), 103103, DOI: 10.1063/1.5037637.

51 P. K. Nayak, S. Mahesh, H. J. Snaith and D. Cahen, Photovoltaic Solar Cell Technologies: Analysing the State of the Art, *Nat. Rev. Mater.*, 2019, **4**(4), 269–285, DOI: 10.1038/s41578-019-0097-0.

52 U. Rau, B. Blank, T. C. M. Müller and T. Kirchartz, Efficiency Potential of Photovoltaic Materials and Devices Unveiled by Detailed-Balance Analysis, *Phys. Rev. Appl.*, 2017, **7**(4), 044016, DOI: 10.1103/PhysRevApplied.7.044016.

53 M. T. Klug, R. L. Milot, R. L. Milot, J. B. Patel, T. Green, H. C. Sansom, M. D. Farrar, A. J. Ramadan, S. Martani, Z. Wang, B. Wenger, J. M. Ball, L. Langshaw, A. Petrozza, M. B. Johnston, L. M. Herz and H. J. Snaith, Metal Composition Influences Optoelectronic Quality in Mixed-Metal Lead-Tin Triiodide Perovskite Solar Absorbers, *Energy Environ. Sci.*, 2020, **13**(6), 1776–1787, DOI: 10.1039/d0ee00132e.

54 F. Hao, C. C. Stoumpos, R. P. H. Chang and M. G. Kanatzidis, Anomalous Band Gap Behavior in Mixed Sn and Pb Perovskites Enables Broadening of Absorption Spectrum in Solar Cells, *J. Am. Chem. Soc.*, 2014, **136**(22), 8094–8099, DOI: 10.1021/ja5033259.

55 V. H. Nguyen, T. K. A. Hoang, Y. Kurokawa and N. Usami, The Impact of Highly Excessive PbI2on the Correlation of MAPbI3perovskite Morphology and Carrier Lifetimes, *J. Mater. Chem. C*, 2020, **8**(41), 14481–14489, DOI: 10.1039/d0tc04071a.

56 H. J. Queisser, Detailed Balance Limit for Solar Cell Efficiency, *Mater. Sci. Eng., B*, 2009, **159–160**, 322–328, DOI: 10.1016/j.mseb.2008.06.033.

57 M. Burgelman, K. Decock, A. Niemegeers, J. Verschraegen and S. Degrave, SCAPS Manual. University of Gent (ELIS), "Most Recent Version.".

58 C. Fei and H. Wang, Age-Induced Recrystallization in Perovskite Solar Cells, *Org. Electron.*, 2019, **68**, 143–150, DOI: 10.1016/j.orgel.2019.02.010.

59 B. Roose, A. Ummadisingu, J. P. Correa-Baena, M. Saliba, A. Hagfeldt, M. Graetzel, U. Steiner and A. Abate, Spontaneous Crystal Coalescence Enables Highly Efficient Perovskite Solar Cells, *Nano Energy*, 2017, **39**, 24–29, DOI: 10.1016/j.nanoen.2017.06.037.

60 M. Minguez-Avellan, O. E. Solis, N. Farinós-Navajas, P. F. Betancur, J. Pascual, T. S. Ripolles, R. Abargues and P. Boix, Ambient Operando Self-Healing in Tin Perovskite Solar Cells, *EES Sol.*, 2026, DOI: 10.1039/D5EL00182J.

61 C. Ran, W. Gao, J. Li, J. Xi, L. Li, J. Dai, Y. Yang, X. Gao, H. Dong, B. Jiao, I. Spanopoulos, C. D. Malliakas, X. Hou, M. G. Kanatzidis and Z. Wu, Conjugated Organic Cations Enable Efficient Self-Healing FASnI3 Solar Cells, *Joule*, 2019, **3**(12), 3072–3087, DOI: 10.1016/j.joule.2019.08.023.

62 Z. Lin, Y. Su, R. Dai, G. Liu, J. Yang, W. Sheng, Y. Zhong, L. Tan and Y. Chen, Ionic Liquid-Induced Ostwald Ripening Effect for Efficient and Stable Tin-Based Perovskite Solar Cells, *ACS Appl. Mater. Interfaces*, 2021, **13**(13), 15420–15428, DOI: 10.1021/acsami.1c01408.